

Spontaneous wettability patterning via creasing instability

Dayong Chen^{a,b}, Gareth H. McKinley^{b,1}, Robert E. Cohen^{a,1}

^aDepartment of Chemical Engineering, Massachusetts Institute of Technology, Cambridge, MA 02139;

^bDepartment of Mechanical Engineering, Massachusetts Institute of Technology, Cambridge, MA 02139;

¹To whom correspondence may be addressed:

Gareth H. McKinley

Email: gareth@mit.edu Phone: (617) 258-0754

Robert E. Cohen

Email: recohen@mit.edu Phone: (617) 253-3777

Keywords: wettability contrast, creasing instability, domain size, morphology, curved surfaces

Abstract

Surfaces with patterned wettability contrast are important in industrial applications such as heat transfer, water collection and particle separation. Traditional methods of fabricating such surfaces rely on microfabrication technologies, which are only applicable to certain substrates and are difficult to scale up and implement on curved surfaces. By taking advantage of a mechanical instability on a polyurethane elastomer film, we show that wettability patterns on both flat and curved surfaces can be generated spontaneously via a simple dip coating process. Variations in dipping time, sample pre-stress and chemical treatment enable independent control of domain size (from about 100 μm to 500 μm), morphology and wettability contrast, respectively. We characterize the wettability contrast using local surface energy measurements via the sessile droplet technique and tensiometry.

Significance

Surfaces with patterned wettability contrast are important in many applications. Traditional fabrication methods rely on microfabrication technologies, which are generally not cost effective, and are difficult to implement on curved surfaces. We show that wettability contrast can be patterned spontaneously on both flat and curved surfaces in a single step process by taking advantage of a reversible creasing instability. Moreover, the domain size, morphology and wettability contrast can be controlled independently, yielding heterogeneous surfaces which show potential for generating high throughput parallel microreactors and for harvesting water from humid air. This mechanical self-assembly approach can also lead to other functional materials beyond wettability patterning.

\body

Introduction

Surfaces that juxtapose local hydrophilic areas with hydrophobic areas show superior performance compared to surfaces with homogeneous wettability in many industrial applications including heat transfer(1), water collecting(2-6), particle separation(7) and microfluidics(8). For instance, developing enhanced water-collecting efficiency has been inspired by the Namib desert beetle, which was reported(2) to have hydrophilic bumps on an overall wax-covered hydrophobic surface. While the hydrophilic bumps reduce the nucleation/coalescence energy of micro-droplets, the overall hydrophobic character of the surface facilitates the spontaneous shedding of water droplets when they grow beyond a certain size.

To achieve surfaces with wettability patterning, traditional fabrication methods such as photolithography and soft lithography have been used. However these methods are generally not cost-effective, not readily scaled up, require multiple process steps, and are difficult to implement on curved surfaces.(3, 9) Recently, mechanical instabilities have been explored as a facile self-assembly approach to endow surfaces with superhydrophobicity(10-12), superhydrophilicity(13), or anisotropic wettability(14). Although mechanical self-assembly provides a low cost route for spontaneous generation of surface patterns, explorations to date have been focused on introducing surface roughness via wrinkling and crumpling instabilities. Here we show that surfaces can be spontaneously patterned with chemical patches with small changes in surface roughness by harnessing a reversible creasing instability(15-17).

A creasing instability develops when a soft polymer network is placed under mechanical compression beyond a certain critical strain, at which point sharp folds spontaneously develop and grow on the deformable free surfaces(18). This process has been linked to the morphology development of the brain(19, 20), electric breakdown of dielectric elastomers(21), and has also been harnessed to prepare switchable surfaces actuated by temperature(22), or electric field(23, 24). Even though the creasing instability develops as a result of large compressive strains, it is elastic in character and reversible(17). Creasing differs from a wrinkling instability in that the surface folds into sharp self-contacts, while in the latter case the surface remains locally smooth. This reversible folding and unfolding of surface self-contacts enables local regions of a creased surface to be reversibly sealed off and then re-opened and can be harnessed to coat soft gels and elastomers with different chemical patterns(22).

By taking advantage of this reversible creasing instability, we show in the present study that wettability patterns on both flat and curved surfaces can be generated spontaneously over large areas via a simple dip coating process. Variations in dipping time, sample pre-stress and chemical treatment, lead to changes in the domain size, the morphology and the wettability contrast of the heterogeneous surface, respectively. We characterize the wettability contrast using sessile droplet

methods and tensiometry. We further show that such scalable and heterogeneous surfaces have potential for generating high throughput parallel microreactors and for harvesting water from humid air.

Results and Discussion

Spontaneous patterning of surfaces with chemical patches

Polyurethane elastomer coatings are generally used to protect surfaces. These coatings are processed from two readily mixable components, with isocyanate groups in the formulation reacting with hydroxyl groups present on the substrates to ensure good adhesion. As shown in Fig. 1a, a polyurethane elastomer film with thickness of ~ 1 mm is coated on a flat polystyrene substrate, which is pretreated with a radio frequency oxygen plasma at 18 W for 5 min immediately prior to coating with the polyurethane, in order to introduce hydroxyl groups on the polystyrene surface. After curing at room temperature for 24 h, the sample is immersed into a solution that contains poly(ethyl methacrylate) (PEMA) / fluorodecyl polyhedral oligomeric silsesquioxane (fluorodecyl POSS) (80:20 by weight) in Asahiklin 225 solvent (a mixture of 3,3-Dichloro-1,1,1,2,2-pentafluoropropane and 1,3-Dichloro-1,1,2,2,3-pentafluoropropane) at a total solid content of 3 wt%. The polyurethane film swells by imbibing solvent molecules. In comparison to a freestanding polyurethane film, which swells freely in three dimensions, the surface-bound polyurethane film can swell only in the direction normal to the substrate. As a result, the swollen film is laterally compressed and is in a state of equibiaxial compression(16, 25). Beyond a critical strain of $\epsilon_{biaxial}^c = 0.25$ (26), creases spontaneously form on the surface of the swollen polyurethane film.

The PEMA/POSS that is dissolved in the Asahiklin solution does not diffuse into the swollen polyurethane elastomer, since diffusion of these molecules into the polyurethane elastomer is thermodynamically unfavorable. The effective network size of the polyurethane elastomer is estimated to be $\xi = (k_b T / G)^{1/3} \approx 1$ nm, smaller than the molecular size of the fluorodecyl POSS molecule and that of the PEMA molecule, estimated to be ~ 3 nm and ~ 25 nm (i.e., the radius of gyration in good solvent condition), respectively, where $k_b T$ is the thermal energy, and $G \approx 1$ MPa is the shear modulus of the polyurethane film. The large interaction parameter expected between the fluorodecyl POSS molecule and the polyurethane molecule also results in a large enthalpic cost for mixing fluorodecyl POSS with polyurethane. Therefore we do not expect fluorodecyl POSS and PEMA molecules to diffuse into the polyurethane elastomeric network. At the polyurethane surface, a depletion layer builds up due to the entropic penalty of polymer confinement(27). As the surface of polyurethane elastomer folds into sharp self-contacts at the creased regions, fluorodecyl POSS and PEMA molecules are squeezed out of the creases, preventing the adsorption of PEMA/POSS in the self-contact regions. When the swollen and creased sample is withdrawn from the PEMA/POSS/Asahiklin solution,

a thin uniform coating layer of PEMA/POSS is deposited on the exposed region of the creased surface as in a typical viscous withdrawal process(28). As shown in SI Fig. S1a, a constant withdrawal speed of $U \approx 0.1 \text{ m/s}$ is applied in the creasing-coating process, corresponding to a capillary number of $Ca = \mu U / \sigma \approx 6.2 \times 10^{-3}$, where $\mu \approx 1 \text{ mPa} \cdot \text{s}$ and $\sigma = 16.2 \text{ mN/m}$ represent the viscosity and surface tension of the coating solution containing 3wt% PEMA/POSS, respectively. According to Landau-Levich-Derjaguin(28, 29), the expected thickness of the coated solution layer is $h \approx 0.94 l_c Ca^{2/3} = 32 \mu\text{m}$, where $l_c = \sqrt{\sigma / \rho g} \approx 1 \times 10^{-3} \text{ m}$ is the capillary length, in which $\rho = 1.6 \times 10^3 \text{ kg/m}^3$ is the density of the coating solution and $g = 9.8 \text{ m/s}^2$ is the gravitational acceleration. Since the 3wt% PEMA/POSS/Asahiklin solution has a solid volume fraction of around 3.5%, rapid evaporation of the volatile solvent results in formation of a uniform dry film of PEMA/POSS on the surface with a thickness of $h_{\text{final}} = 0.035h \approx 1 \mu\text{m}$. This predicted dry film thickness of PEMA/POSS layer is confirmed experimentally by scanning electron microscopy (SEM) imaging of the cross section (SI Fig. S1b). The cross-sectional image also reveals the clear boundary between the PEMA/POSS layer and the polyurethane elastomer, confirming that no PEMA or POSS molecules diffuse into the polyurethane elastomer. The subsequent slow deswelling of the polyurethane substrate below causes the unfolding of creases, revealing the uncoated self-folding regions (Fig. 1a). Increased amounts of the PEMA/POSS coating solution are trapped at the edge of these folds as a result of contact line pinning and the coffee ring effect(30), leaving additional material deposited at the edge of the creases, as indicated by the darker rims around the uncoated regions shown in Fig. 1b.

While this creasing/coating process generates patterned surfaces with regions of chemical contrast, it produces only minimal surface topographical modification. As shown in SI Fig. S2, a 3D surface profile is obtained by performing a surface scan on the coated polyurethane film (swollen in PEMA/POSS solution for 100 s before withdrawal) with a stylus profilometer. Multiple rings are observed around the unfolded crease, resulting from the competition between dewetting and contact line pinning(31). The root mean square roughness is $R_q = 380 \text{ nm}$, much smaller than the lateral length scale of the chemical patches, which are on the order of $100 \mu\text{m}$. The chemical contrast on the polyurethane surface is characterized via energy dispersive spectroscopy (EDS). As seen in Fig. 1c, the exposed area (outside the self-creased domains) has much higher fluorine element content while the creased regions have minimal fluorine content. This patterned hydrophobic fluorodecyl POSS coating leads to pronounced local surface wettability contrast, which will be characterized and discussed in later sections. PEMA acts as a compatibilizing layer between the POSS and the polyurethane surface that enhances the adhesion of hydrophobic fluorodecyl POSS molecules to the polyurethane elastomer(32). The low energy POSS molecules reside preferentially at the free surface while the PEMA

chains interact with the polyurethane elastomer, creating a strong interface. We confirm the strong adhesion by performing a simple peel adhesion test (SI Fig. S3).

The success of this wettability patterning approach relies on three factors: swelling of the polyurethane elastomer film beyond the critical strain for creasing; the low surface tension of the PEMA/POSS blend; and the fast evaporation of the volatile solvent (Asahiklin). In another case, we swell a polydimethylsiloxane (PDMS) elastomer film in a solution containing 3 wt% poly(ethyl glycol) (PEO) in chloroform. Creases are formed and chloroform is volatile, however patterned wettability is not observed. The hydrophilic PEO has a much higher surface tension of 43 mN/m compared to the value for PDMS of 20 mN/m(33), leading to dewetting upon crease unfolding (SI Movie 1 and Fig. S4).

Modulation of the size and morphology of wettability patterns

Both the size and shape of wettability patterns influence performance in applications such as heat transfer(1) and water harvesting(4, 5). In this section, we show that the size and morphology of the wettability contrast pattern can be controlled independently.

The swelling of elastomers in a solvent is a poroelastic process(34). The swollen layer thickness H is governed by the diffusive dynamics of the solvent. In the creasing process, the spacing W between neighboring creases is proportional to the thickness of the swollen layer since that is the only relevant length scale(16). As shown in SI Movie 2, the small creases that initially nucleate subsequently coarsen as the swollen layer grows in thickness. The spacing of the creases (W) can be measured through image analysis. In Fig. 2a, W^2 is plotted against the dipping time and the linearity of the plot supports the diffusive nature of the phenomenon, allowing us to obtain an effective diffusion constant $D_{eff} = W^2 / t = 7.69 \times 10^{-10} \text{ m}^2 / \text{s}$. Given that the spacing of the creases (W) scales with the initial thickness of the swollen layer (\tilde{H}) by a ratio of $W / \tilde{H} \approx 2 - 2.5$ (16), the effective diffusion constant D_{eff} is reduced by a factor of $(W / \tilde{H})^2 \approx 4 - 6.25$ which agrees well with the diffusivity of $D \approx 1.3 \times 10^{-10} \text{ m}^2 / \text{s}$ resulting from tracking the thickness change during the swelling of a free-standing polyurethane film (see SI Fig. S5). Guided by the diffusion analysis, non-coated hydrophilic regions of different sizes can therefore be achieved by controlling the swelling time. While micrographs in Fig. 2b show patches of 3 different sizes ranging from 100 μm to 500 μm , we note that this process has the potential to generate smaller patterns, down to the tens of nanometer scale(35, 36). Successful processing of very small patterns relies on a thin polyurethane layer, the thickness of which imposes an upper bound for the evolving pattern size, and on a very fast solvent evaporation rate to prevent the viscous coating solution from migrating laterally onto the uncoated regions during the simultaneous deswelling of the elastomeric film and the unfolding of creases.

Constrained swelling always leads to equibiaxial compression in the polyurethane elastomer coating. The polyurethane film has a swelling ratio of $\lambda_0 = 1.47$ (measured from the change in dimensions of a free standing polyurethane film) in 3wt% PEMA/POSS/Asahiklin solution. Taking the free swelling state as the reference state, the compressive strains induced in the film by constrained swelling are $\varepsilon_x = \varepsilon_y = 1 - 1/\lambda_0 = 0.32$, which is above the critical strain of $\varepsilon_{biaxial}^c = 0.25$ required for creases to form(26). In Fig. 3, the experimental image on the bottom shows a similar morphology to that on the top based on the theoretical predictions (highlighted by the blue square).(37) Globally, the patterns that form are randomly oriented due to the in-plane stress symmetry, while locally the short striped creases are arranged in a mostly perpendicular fashion to their neighbors, to most effectively release the compressive energy in plane. Breaking the in-plane stress symmetry yields patterns with different morphology(37). Specifically, we can put the polyurethane elastomer film under pre-compression by gluing it to a pre-stretched substrate and subsequently releasing the pre-stretch, followed by immersing it in the PEMA/POSS/Asahiklin solution. Working on jointly, the amplitude of pre-compression and the swelling ratio determine the final stress state in the polyurethane elastomer, leading to creases with different morphologies. Applying a pre-compression of $\lambda'_x = 0.85$ in the x-direction, followed by subsequent swelling lead to a strain state with the ratio of in-plane strains $\varepsilon_y / \varepsilon_x = 0.64$ (See SI Fig. S6). As highlighted by the red square in Fig. 3, the micrograph on the bottom shows long stripe patterns along the less compressed (y) direction, in good agreement with the corresponding range of theoretical predictions shown on the top. The two examples provided here demonstrate that the morphology of our wettability patterning can be tuned by controlling the initial stress state in the elastomeric surface layer.

Characterization of the wettability of the patterned surfaces

We next characterize the wettability of the patterned surfaces using the sessile droplet technique and tensiometry. Water contact angle were measured on the uncoated polyurethane surface and a surface uniformly coated with PEMA/POSS via the sessile droplet technique. The advancing and receding contact angles for water on the uncoated polyurethane are $\theta_a = 88 \pm 2^\circ$ and $\theta_r = 32 \pm 1^\circ$, respectively. On the uniformly coated PEMA/POSS surface prepared by spin coating the 3 wt% Asahiklin solution, the advancing and receding contact angles for water are $\theta_a = 124 \pm 1^\circ$ and $\theta_r = 118 \pm 1^\circ$ respectively, in good agreement with a previous study(32). We note that elastocapillarity can affect the apparent contact angle of liquid drops on soft elastomers(38). The polyurethane elastomer used here has a shear modulus of $G_{PU} \approx 1$ MPa and the water surface tension is $\gamma_{LV} = 72.8$ mN/m, so the elastocapillary length is of order $\gamma_{LV} / G_{PU} \approx 70$ nm, much smaller than the radius of

the sessile droplet. For this relatively stiff polyurethane elastomer, elastocapillarity has a negligible influence on the apparent contact angle(39).

To visualize the patterned wettability contrast directly on the polyurethane surface, we observe a 20 μl droplet rolling down a patterned surface tilted at 60°. As shown in SI Movie 3, capillary fingers continuously form and pinch off in the hydrophilic regions as the water droplet recedes along the inclined surface. The capillary finger breakup as well as the average surface contact angle can be measured by tensiometry. As illustrated in Fig. 4a, in these tensiometric experiments force and relative position data are collected while a container of probe liquid is raised and lowered at a constant velocity such that the liquid contact line advances (or recedes) across the solid surface at a controlled velocity. In the quasi-static limit, when viscous forces are negligible, the net force acting on the sample results from a combination of interfacial and buoyant forces and is given by $F = p\gamma_{LV} \cos\theta - \rho_L gAd$, where p , γ_{LV} , θ , ρ_L , g , A and d represent the perimeter length of the cross-section, the liquid surface tension, the liquid-surface contact angle, the liquid density, the gravitational acceleration, the cross-sectional area and the immersion depth, respectively(40). Three advancing and receding cycles are recorded at an immersion velocity of 0.1 mm/s (Fig. 4a). Linear regression to the advancing and receding force measurements gives rise to the average advancing and receding angles. While the measured receding contact angle is $104 \pm 2^\circ$, there is a decrease of advancing contact angle from $147 \pm 1^\circ$ in the first advancing cycle to $136 \pm 3^\circ$ in the second and third advancing cycles, reflecting a small amount of water absorption by the polyurethane elastomer. The patterned surface has a larger water advancing contact angle compared to the flat PEMA/POSS surface, due to the introduction of surface roughness, following the swelling/deswelling/evaporation process.

In these experiments, the meniscus advances at $U=0.1$ mm/s, corresponding to a capillary number of $Ca = \mu U / \gamma_{LV} = 1.4 \times 10^{-6}$, where μ represents the viscosity of the liquid. At this small capillary number, capillary fingers form and break up, without leaving visible droplets in the hydrophilic regions. Such stick-slip behavior of a moving contact line on chemically patterned surfaces has been observed before both computationally(41) and experimentally(42). The stick-slip capillary finger formation and breakup is captured in the advancing and receding force-displacement curves as sawtooth patterns. Fig. 4b shows an enlarged view of the first receding force curve. 1D Fourier transformation of this signal yields a characteristic wavelength of 300 μm , corresponding well to the average spacing of creases as shown in the inset of Fig. 4b. The agreement between the periodicity of the sawtooth patterns and the average spacing of creases is further confirmed in SI Fig. S7, where a sample with an 800 μm average spacing of creases is tested under the same conditions. However, as recorded in SI Movie 4, when the patterned sample is withdrawn from a water bath at a speed of $U=40$ mm/s, corresponding to a much larger capillary number of $Ca=5.6 \times 10^{-4}$, the elongated capillary fingers

leave a microdroplet in each hydrophilic domain. Fig. 4c and 4d show that brine (1.37 M sodium chloride) and oil microdroplets can be deposited in the hydrophilic regions through this process, suggesting that this simple immersion/emersion process can be utilized to prepare microreactors in parallel. We demonstrate this concept in SI Fig. S8 by synthesizing magnetic microparticles. The deposited microdroplets have radii on the order of tens of microns, which evaporate quickly. The relatively lower vapor pressure of brine solutions allows for reliable measurement of the size of the deposited droplets through optical microscopy. The diameters of brine microdroplets deposited in the hydrophilic regions at a withdrawal speed of $U = 40$ mm/s are narrowly distributed in size with a mean diameter of 38 ± 4 μm (SI Fig. S9). We note that the volume (V) of each deposited microdroplet should be a function of the capillary number (Ca), the receding contact angle (θ_r) and the characteristic length (L) of the hydrophilic domain through Landau-Levich dynamics(43). However, the detailed characterization of the appropriate functional form $V = f(Ca, \theta_r, L)$ is beyond the scope of the current study. Patterning droplets on a surface can also be influenced by other factors such as substrate stiffness(44) and surface roughness(45, 46). Our coating process generates a substrate stiffness contrast. While the uncoated polyurethane has a shear modulus of $G_{PU} \approx 1$ MPa, the coated 1 μm PEMA/POSS layer has a shear modulus of $G_{PEMA/POSS} \approx 1$ GPa (47). The deposited droplets have radii on the order of tens of microns, 3 and 6 orders of magnitude larger than the elastocapillary lengths on polyurethane substrate ($\gamma_{LV}/G_{PU} \approx 70$ nm) and on PEMA/POSS layer ($\gamma_{LV}/G_{PEMA/POSS} \approx 0.7$ nm), respectively. Therefore substrate stiffness effects or “durotaxis” is not to be expected in our current experiments(44). Surface roughness can also result in stick-slip motion in moving contact lines(45, 46). The rough corners and sharp edges can cause pinning of contact lines, and subsequent release of pinning from these surface features leads to sudden slipping of the contact lines. Our coated surface has a root mean square roughness of $R_q = 380$ nm, which is 2-3 orders of magnitude smaller than the lateral length scale (ca. 100-500 μm) of the hydrophilic regions, implying the effect of surface roughness is probably small. But quantitative deconvolution of the effect of the wettability contrast from the effect of the surface roughness on microdroplet deposition in the current experiment is not possible with the information available.

The wettability contrast between the coated and the uncoated regions can be enhanced by improving the hydrophilicity of the polyurethane surface prior to the coating step. A three-minute oxygen plasma treatment (radio frequency plasma at 18 W) reduces the water advancing angle on the polyurethane surface from $\theta_a = 88 \pm 2^\circ$ to $58 \pm 1^\circ$, and the receding angle from $\theta_r = 32 \pm 1^\circ$ to $8 \pm 2^\circ$, as measured by the sessile droplet technique. Fig. 4e and 4f show a surface patterned with long

stripes by applying a pre-compression of $\lambda'_x = 0.85$ prior to the coating process, as discussed in the previous section. For the polyurethane surface without oxygen plasma treatment (Fig. 4e), the water filaments that develop during withdrawal break into small ellipsoidal drops due to dewetting and the Rayleigh-Plateau instability, whereas on the oxygen plasma treated surface (Fig. 4f), water filaments remain as continuous rivulets in good registry with the hydrophilic regions. While the oxygen plasma treatment enhances the wetting contrast, it also tends to slightly alter the morphology of creases and the wettability patterns (SI Fig. S10), probably due to changes in the surface roughness, surface energy and the mechanical properties of the polyurethane induced by the oxygen plasma (48, 49).

We probe the local modifications to the wettability by performing local contact angle measurements; delivering water microdroplets (volume $\leq 0.02 \mu\text{L}$) precisely to different regions (SI Fig. S11). The local measurements show good agreement with water contact angles measured previously on bulk surfaces, confirming that the coating process does not significantly change the water contact angles in the uncoated creased regions.

Water condensation on patterned surfaces

One of the motivations for patterning surfaces with wettability contrast is to enhance water-collection efficiency. While Namib desert beetles are believed to use hydrophilic bumps distributed on a hydrophobic background to harvest fog droplets (2), it is also argued that enhanced dew condensation can be another potential mechanism for these beetles to collect water (50). We have also investigated the water condensation behavior on our patterned surfaces. As shown in SI Movie 5 and Fig. 5, a patterned surface is equilibrated to -20°C in a freezer for 30 min prior to performing a water condensation experiment at 21°C and 40% relative humidity. Water condensation from the air to the cold surface is monitored *in-situ* by an optical microscope operated in reflection mode. Initially, tiny water droplets condense on the entire surface due to the large subcooling. These droplets grow, coarsen and coalesce much faster in the hydrophilic regions. The free energy barrier ΔG for the formation of a water nucleus on a flat surface depends strongly on the contact angle θ : $\Delta G = \pi\gamma_{LV}r_c^2(2 - 3\cos\theta + \cos^3\theta)/3$, where r_c is the critical radius of a water nucleus (51). The critical radius in the current experiment is calculated to be $r_c = 0.75 \text{ nm}$ using the Kelvin equation: $\ln(S) = 2\gamma_{LV}/(n_L k_b T r_c)$ (52), where $S=5$ is the saturation ratio of water vapor pressure in the experiment; defined by the ratio of water vapor pressure in the environment to the dew point at the cold surface, n_L is the number of molecules per unit volume of water, and $k_b T$ is the thermal energy. The nucleation rate J depends on the nucleation energy barrier in an inverse exponential form: $J = J_0 \exp(-\Delta G/k_b T) = J_0 \exp(-\pi\gamma_{LV}r_c^2(3\cos\theta - 2 - \cos^3\theta)/3k_b T)$, where J_0 is a kinetic constant. Therefore based on this expression, the nucleation

rate in the more hydrophilic regions ($\theta_{adv} = 88^\circ$) is ~ 10 orders of magnitude higher than that in the coated regions ($\theta_{adv} = 127^\circ$). Additional materials deposited at the rim of the hydrophilic regions increase the roughness, and therefore the level of hydrophobicity at the rim. So the tiny water droplets that initially condense at the rim quickly coalesce to form droplets that sit on the nearby hydrophilic regions. The regions near the boundaries of the creases thus reflect more light, and appear to turn white quickly, an observation that can be explained by a mobile coalescence mechanism on a superhydrophobic surface. It is known that coalescence of microdroplets condensed on a superhydrophobic surface can induce out-of-plane jumping, which is powered by the released surface energy upon drop coalescence(53). This type of mobile coalescence mechanism allows only condensed droplets with diameters smaller than $10\text{ }\mu\text{m}$ to sit on a superhydrophobic surface(53). As illustrated in SI Fig. S12, while microdroplets larger than this critical size at the rim jump and coalesce to form droplets in the nearby hydrophilic regions, water microdroplets still remain in the flat hydrophobic regions and scatter light. Therefore these flat hydrophobic regions appear dark while the rim regions appear white in the optical micrographs (Fig. 5). The difference in water condensation rate in different regions on the patterned surface offers potential for using such patterned surfaces to enhance the efficiency of harvesting and collection of dew water condensing from humid air (See SI).

Spontaneous patterning on curved surfaces

Traditional techniques for patterning surfaces with spatial wettability contrast include vapor deposition(8), photolithography(3), and soft lithography(54, 55). While photolithography can only be used to pattern flat substrates, soft lithography using flexible molds or masks fabricated via photolithography can work on cylindrical or conical surfaces, i.e., curved surfaces with zero Gaussian curvature(54, 55). However, such techniques cannot be applied to surfaces with non-zero Gaussian curvature such as spherical or saddle surfaces. Essentially, the flexible molds or masks in use have zero Gaussian curvature. Distortions including stretching and compression have to be applied when a flat mask is mapped onto a surface with a non-zero Gaussian curvature(56). A micro-spraying system offers the possibility to operate and pattern wettability to arbitrarily curved surfaces(57), however, it requires precise and sophisticated maneuvering of the spray head in three dimensions and should be difficult and costly to scale up.

Our new crease coating approach includes the capability of producing patterned wettability on any arbitrarily curved surface and on a wide variety of materials. As shown in Fig. 6, both a cylindrical surface (Fig. 6a) and a spherical surface (Fig. 6b) can be patterned readily. Our approach relies on the conformal coating of arbitrary surfaces with a well-adhered layer of polyurethane elastomer. Chemical reactivity with hydroxyl groups present on the surface of a variety of substrate materials ensures good adhesion of the polyurethane elastomer layer. Therefore, this

patterning approach works on a variety of materials, such as plasma treated polystyrene mentioned in previous sections, oxidized steel (Fig. 6a) and glass (Fig. 6b). The patterning is primarily a chemical process with the introduction of very small incremental surface roughness as discussed previously. Consequently, it only slightly reduces light transmission when applied to a transparent substrate. As shown in Fig. 6b, the coated spherical glass lens remains highly transparent.

Conclusions

In summary, exploiting the reversible creasing instability of swollen elastomers provides a facile self-assembly approach to spontaneously pattern both flat and curved surfaces with wettability contrasts having a characteristic feature scale from about 100 μm to 500 μm . The patterning is primarily a chemical process with little change in the surface roughness. Variations in dipping time, pre-stress and chemical treatment, allow for independent control of the domain size, the morphology and the wettability contrast, respectively. Such heterogeneous surfaces show potential for constructing high throughput parallel microreactors and for harvesting and collecting water from humid air.

Methods

All the patterned samples with wettability contrast are prepared by immersing substrate-bonded polyurethane films in a solution that contains 3 wt% PEMA /fluorodecyl POSS (80:20 by wt) in Asahiklin solvent (AK225). The polyurethane film-coated substrates are withdrawn vertically at a speed of $U \approx 0.1$ m/s from the coating solution after immersing them for a certain period of time, and left in a fume hood to evaporate residual solvent, leading to simultaneous deswelling of the polyurethane film and exposure of the uncoated self-contacting regions. More details can be found in the SI text.

Acknowledgements

The work is financially supported by the Army Research Office through Contract W911NF-13-D-0001.

References:

1. Betz AR, Xu J, Qiu H, Attinger D (2010) Do surfaces with mixed hydrophilic and hydrophobic areas enhance pool boiling? *Appl Phys Lett* 97(14):141909.
2. Parker AR, Lawrence CR (2001) Water capture by a desert beetle. *Nature* 414(6859):33-34.
3. Zhai L, *et al.* (2006) Patterned superhydrophobic surfaces: toward a synthetic mimic of the Namib Desert beetle. *Nano Lett* 6(6):1213-1217.
4. Garrod R, *et al.* (2007) Mimicking a *Stenocara* beetle's back for microcondensation using plasmachemical patterned superhydrophobic-superhydrophilic surfaces. *Langmuir* 23(2):689-693.

5. Bai H, *et al.* (2014) Efficient Water Collection on Integrative Bioinspired Surfaces with Star - Shaped Wettability Patterns. *Adv Mater* 26(29):5025-5030.
6. Thickett SC, Neto C, Harris AT (2011) Biomimetic surface coatings for atmospheric water capture prepared by dewetting of polymer films. *Adv Mater* 23(32):3718-3722.
7. Zhang R, Koplik J (2012) Separation of nanoparticles by flow past a patterned substrate. *Phys Rev E* 85(2):026314.
8. Gau H, Herminghaus S, Lenz P, Lipowsky R (1999) Liquid morphologies on structured surfaces: from microchannels to microchips. *Science* 283(5398):46-49.
9. Tian D, Song Y, Jiang L (2013) Patterning of controllable surface wettability for printing techniques. *Chem Soc Rev* 42(12):5184-5209.
10. Zang J, *et al.* (2013) Multifunctionality and control of the crumpling and unfolding of large-area graphene. *Nat Mater* 12(4):321-325.
11. Manna U, Carter MC, Lynn DM (2013) “Shrink-to-fit” superhydrophobicity: thermally - induced microscale wrinkling of thin hydrophobic multilayers fabricated on flexible shrink - wrap substrates. *Adv Mater* 25(22):3085-3089.
12. Li Y, Dai S, John J, Carter KR (2013) Superhydrophobic surfaces from hierarchically structured wrinkled polymers. *ACS Appl Mater Interfaces* 5(21):11066-11073.
13. Bahners T, Prager L, Kriehn S, Gutmann JS (2012) Super-hydrophilic surfaces by photo-induced micro-folding. *Appl Surf Sci* 259:847-852.
14. Chung JY, Youngblood JP, Stafford CM (2007) Anisotropic wetting on tunable micro-wrinkled surfaces. *Soft Matter* 3(9):1163-1169.
15. Tanaka T, *et al.* (1987) Mechanical instability of gels at the phase transition. *Nature* 325(6107):796-798.
16. Trujillo V, Kim J, Hayward RC (2008) Creasing instability of surface-attached hydrogels. *Soft Matter* 4(3):564-569.
17. Chen D, Jin L, Suo Z, Hayward RC (2014) Controlled formation and disappearance of creases. *Mater Horiz* 1(2):207-213.
18. Cai S, Chen D, Suo Z, Hayward RC (2012) Creasing instability of elastomer films. *Soft Matter* 8(5):1301-1304.
19. Hohlfeld E, Mahadevan L (2011) Unfolding the sulcus. *Phys Rev Lett* 106(10):105702.
20. Tallinen T, Chung JY, Biggins JS, Mahadevan L (2014) Gyrification from constrained cortical expansion. *Proc Natl Acad Sci USA* 111(35):12667-12672.
21. Wang Q, Zhang L, Zhao X (2011) Creasing to cratering instability in polymers under ultrahigh electric fields. *Phys Rev Lett* 106(11):118301.
22. Kim J, Yoon J, Hayward RC (2010) Dynamic display of biomolecular patterns through an elastic creasing instability of stimuli-responsive hydrogels. *Nat Mater* 9(2):159-164.

23. Wang Q, Tahir M, Zang J, Zhao X (2012) Dynamic electrostatic lithography: multiscale on - demand patterning on large-area curved surfaces. *Adv Mater* 24(15):1947-1951.
24. Xu B, Hayward RC (2013) Low-voltage switching of crease patterns on hydrogel surfaces. *Adv Mater* 25(39):5555-5559.
25. Guvendiren M, Burdick JA, Yang S (2010) Solvent induced transition from wrinkles to creases in thin film gels with depth-wise crosslinking gradients. *Soft Matter* 6(22):5795-5801.
26. Hong W, Zhao X, Suo Z (2009) Formation of creases on the surfaces of elastomers and gels. *Appl Phys Lett* 95(11):111901.
27. De Gennes P (1981) Polymer solutions near an interface. adsorption and depletion layers. *Macromolecules* 14(6):1637-1644.
28. Landau L, Levich B (2012) Dragging of a liquid by a moving plate. *Acta Physicochimica (USSR)* 17:42-54.
29. Quéré D (1999) Fluid coating on a fiber. *Annu Rev Fluid Mech* 31(1):347-384.
30. Deegan RD, et al. (1997) Capillary flow as the cause of ring stains from dried liquid drops. *Nature* 389(6653):827-829.
31. Deegan RD (2000) Pattern formation in drying drops. *Phy Rev E* 61(1):475.
32. Meuler AJ, et al. (2011) Examination of wettability and surface energy in fluorodecyl POSS/polymer blends. *Soft Matter* 7(21):10122-10134.
33. Mark JE (2009) *Polymer Data Handbook* (Oxford University Press).
34. Cai S, Hu Y, Zhao X, Suo Z (2010) Poroelasticity of a covalently crosslinked alginate hydrogel under compression. *J Appl Phys* 108(11):113514.
35. Ortiz O, Vidyasagar A, Wang J, Toomey R (2010) Surface instabilities in ultrathin, cross-linked poly (N-isopropylacrylamide) coatings. *Langmuir* 26(22):17489-17494.
36. Brooks K, Razavi MJ, Wang X, Locklin J (2015) Nanoscale Surface Creasing Induced by Post-Polymerization Modification. *ACS Nano* 9(11):10961-10969.
37. Tallinen T, Biggins JS, Mahadevan L (2013) Surface sulci in squeezed soft solids. *Phys Rev Lett* 110(2):024302.
38. Marchand A, Das S, Snoeijer JH, Andreotti B (2012) Contact angles on a soft solid: from Young's law to Neumann's law. *Phys Rev Lett* 109(23):236101.
39. Style RW, et al. (2013) Universal deformation of soft substrates near a contact line and the direct measurement of solid surface stresses. *Phys Rev Lett* 110(6):066103.
40. Kleingartner JA, Lee H, Rubner MF, McKinley GH, Cohen RE (2013) Exploring the kinetics of switchable polymer surfaces with dynamic tensiometry. *Soft Matter* 9(26):6080-6090.
41. Wang X-P, Qian T, Sheng P (2008) Moving contact line on chemically patterned surfaces. *J Fluid Mech* 605:59-78.
42. Varagnolo S, et al. (2013) Stick-slip sliding of water drops on chemically heterogeneous surfaces. *Phys Rev Lett* 111(6):066101.
43. Snoeijer JH, Andreotti B (2013) Moving contact lines: scales, regimes, and dynamical transitions. *Annu Rev Fluid Mech* 45:269-292.

44. Style RW, et al. (2013) Patterning droplets with durotaxis. *Proc Natl Acad Sci USA* 110(31):12541-12544.
45. Savva N, Kalliadas S, Pavliotis GA (2010) Two-dimensional droplet spreading over random topographical substrates. *Phys Rev Lett* 104(8):084501.
46. Sui Y, Ding H, Spelt PD (2014) Numerical simulations of flows with moving contact lines. *Annu Rev Fluid Mech* 46:97-119.
47. Li X, McKenna GB (2012) Considering viscoelastic micromechanics for the reinforcement of graphene polymer nanocomposites. *ACS Macro Lett* 1(3):388-391.
48. Sanchis M, Calvo O, Fenollar O, Garcia D, Balart R (2007) Surface modification of a polyurethane film by low pressure glow discharge oxygen plasma treatment. *J Appl Polym Sci* 105(3):1077-1085.
49. Gorna K, Gogolewski S (2003) Molecular stability, mechanical properties, surface characteristics and sterility of biodegradable polyurethanes treated with low-temperature plasma. *Polym Degrad Stab* 79(3):475-485.
50. Guadarrama-Cetina J, et al. (2014) Dew condensation on desert beetle skin. *Eur Phys J E* 37(11):1-6.
51. Varanasi KK, Hsu M, Bhate N, Yang W, Deng T (2009) Spatial control in the heterogeneous nucleation of water. *Appl Phys Lett* 95(9):094101.
52. Butt H-J, Graf K, Kappl M (2006) *Physics and Chemistry of Interfaces* (John Wiley & Sons).
53. Boreyko JB, Chen C-H (2009) Self-propelled dropwise condensate on superhydrophobic surfaces. *Phys Rev Lett* 103(18):184501.
54. Li Z, et al. (2009) Hybrid nanoimprint-soft lithography with sub-15 nm resolution. *Nano Lett* 9(6):2306-2310.
55. Kim J, Takama N, Kim B, Fujita H (2009) Optical-softlithographic technology for patterning on curved surfaces. *J Micromech Microeng* 19(5):055017.
56. Gauss KF (1827) *General investigations of curved surfaces of 1827 and 1825*, translated by Morehead JC and Hildebeitel AM (The Princeton University Library, Princeton).
57. De Silva MN, Paulsen J, Renn MJ, Odde DJ (2006) Two-step cell patterning on planar and complex curved surfaces by precision spraying of polymers. *Biotechnol Bioeng* 93(5):919-927.
58. Yoon J, Cai S, Suo Z, Hayward RC (2010) Poroelastic swelling kinetics of thin hydrogel layers: comparison of theory and experiment, *Soft Matter* 6(23): 6004-6012.

Figure legends

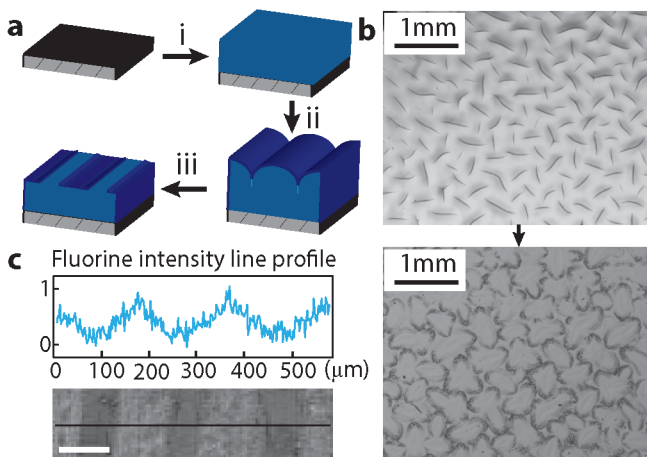


Fig. 1 Spontaneous surface patterning via reversible creasing instability. (a) The procedure of patterning consists of three steps: i) coating substrate with a polyurethane elastomer film; ii) unidirectional swelling of the geometrically constrained polyurethane film in a solution containing poly(ethyl methacrylate)/fluorodecyl POSS in Asahiklin solvent, leading to creases formed on the surface; and iii) withdrawing the sample from the coating solution resulting in a PEMA/POSS coating to the exposed regions, and evaporation of Asahiklin solvent causing the polyurethane film to deswell, which leads to unfolding of the creases and exposure of the uncoated self-contact regions. (b) Optical micrographs showing creases observed on the polyurethane film surface (top) and a patterned surface via reversible creasing (bottom). (c) A fluorine element intensity line profile by energy dispersive spectroscopy (EDS) showing the deposition of hydrophobic fluorodecyl POSS molecules on the exposed regions (Scale bar: 100 μm).

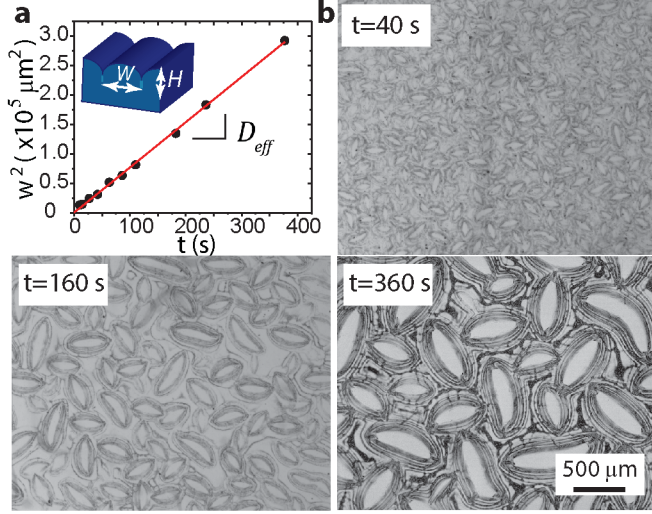


Fig. 2 Modulating the size of patterned patches by controlling the swelling time. (a) The spacing (W) between neighboring creases is proportional to the swollen layer thickness (H), which is controlled by the swelling time (t). An effective diffusion constant ($D_{eff} = 7.69 \times 10^{-10} \text{ m}^2/\text{s}$) for the swelling of the elastomer by the solvent can be obtained by plotting W^2 as a function of t . (b) Micrographs showing three different pattern sizes resulting from three different swelling times.

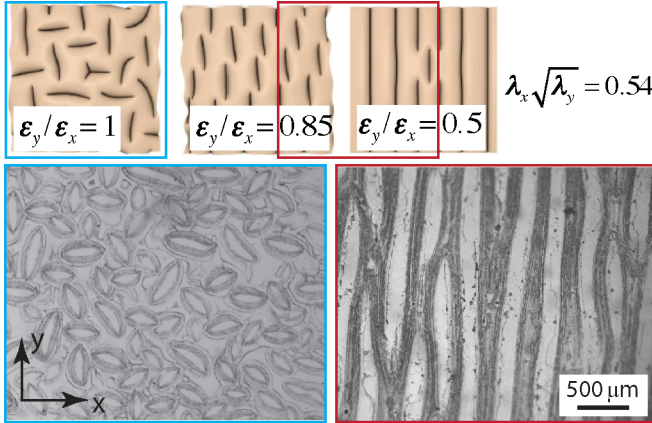


Fig. 3 Modulating the morphology of patterned patches by pre-compression. Top row; images show the predicted morphology of creases at different stress states, reproduced from Ref. (37) with permission from the American Physical Society(2013). Bottom row; micrographs show the morphology of patterned patches obtained under different stress states (left: $\epsilon_y/\epsilon_x = 1$; right: $\epsilon_y/\epsilon_x = 0.62$), in good agreement with the theoretical results at similar stress states on the left, as highlighted in the red and blue squares. The level of overall compression denoted by $\lambda_x\sqrt{\lambda_y}$ in experiments is close to that (0.54) in the theoretical results.

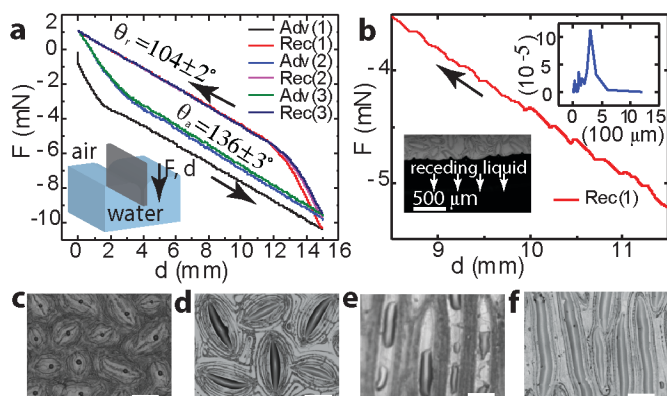


Fig. 4 Tensiometry measurements of the patterned surfaces and formation of microdroplets due to capillary finger breakup. (a) Tensiometry measurements on a patterned surface for three advancing and receding cycles. (b) An enlarged view of the tensiometric force curve for the first receding measurement shows sawtooth waves corresponding to the stick-slip of capillary fingers at the receding contact line. The upper inset figure shows the power spectrum of a 1D Fourier transform of the sawtooth waves, with a primary peak at 300 μm , in good agreement with the spacing between creases shown in the lower left inset optical micrograph. (c) Brine (1.37 M sodium chloride) and (d) hexadecane microdroplets deposited on hydrophilic regions due to capillary finger breakup. (e) Water rivulets breaking into short ellipsoidal droplets on non-treated hydrophilic regions. (f) Continuous water rivulets adhere to oxygen plasma-treated hydrophilic regions with high fidelity. Scale bars represent 250 μm .

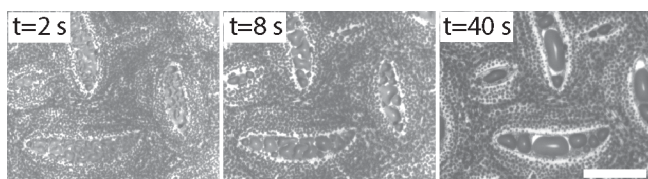


Fig. 5 Optical micrographs showing the temporal evolution of condensation of water droplets from the air (at room temperature (21 $^{\circ}\text{C}$) and 40% relative humidity) onto a cold patterned surface (-20 $^{\circ}\text{C}$). The volume of the water droplets deposited on the uncoated, hydrophilic regions is many orders of magnitude higher than the volume of water microdrops deposited on the coated hydrophobic regions, reflecting the influence of local patterning in the surface wettability on local droplet nucleation rate. Scale bar represents 200 μm .

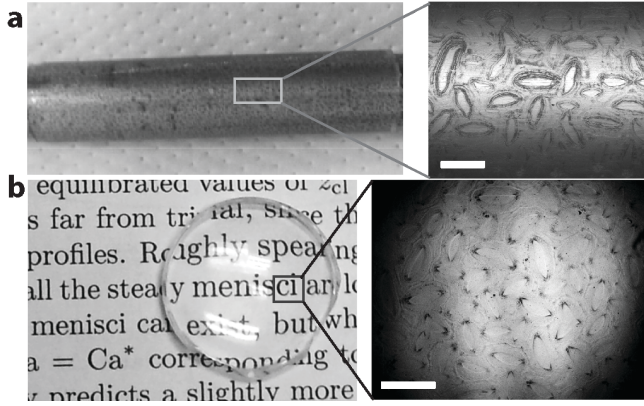


Fig. 6 Spontaneous wettability patterning on curved surfaces: (a) a cylindrical steel rod surface (15 mm in diameter), which has a mean curvature of $H = 1/2(1/R_1 + 1/R_2) = 0.067 \text{ mm}^{-1}$ and a Gaussian curvature of $K = 1/(R_1 R_2) = 0$, and (b) a spherical glass lens surface (8 mm in radius, 2 mm in thickness at the apex of the lens), with $H = 0.125 \text{ mm}^{-1}$ and $K = 0.0156 \text{ mm}^{-2}$. Scale bars represent 500 μm. (R_1 and R_2 are the two principal radii of a curved surface.)